Catalysis Today 199 (2013) 8–14

Contents lists available at SciVerse ScienceDirect

Catalysis Today

journal homepage: www.elsevier.com/locate/cattod

Naphthalene derivatized TiO_2–carbon hybrid materials for efficient photocatalytic splitting of water

Sreenivasan Koliyat Parayil, Harrison S. Kibombo, Ranjit T. Koodali*

Department of Chemistry, University of South Dakota, Vermillion, SD 57069, USA

ARTICLE INFO

Article history:
Received 11 November 2011
Received in revised form 18 January 2012
Accepted 5 February 2012
Available online 3 March 2012

Keywords:
TiO_2
Dihydroxynaphthalene
Pyrolysis
Carbon
Photocatalysis
Hydrogen generation

ABSTRACT

We report a facile approach for the synthesis of TiO_2–Carbon (C) hybrid formed by a ligand-to-metal charge transfer (LMCT) complexation between a small organic molecule precursor, 2,3-dihydroxynaphthalene (DN) and TiO_2 nanomaterial. The resultant photocatalysts were characterized by powder X-ray diffraction (XRD), surface area and porosity analysis, Raman spectroscopy, diffuse reflectance spectroscopy (DRS), photoluminescence (PL) spectroscopy, transmission electron microscopy (TEM), and by X-ray photoelectron spectroscopy (XPS). Carbonization by N_2 pyrolysis at 800 °C altered the physical properties of the TiO_2 as evidenced by the increase in the surface area of TiO_2 from 6.5 $m^2\ g^{-1}$ to 12.5 $m^2\ g^{-1}$ and fluorescence quenching of TiO_2 emission. The photocatalytic performances of these TiO_2–C hybrid materials were evaluated by calculating the amount of hydrogen evolved from the decomposition of water under solar simulated illumination. A marked improvement was observed from ~0 to 2.6 $\mu mol/g_{TiO_2}/h$ evolved from the bare TiO_2-0 and TiO_2–C-240 composites, respectively. These results suggested that anchoring of C onto the TiO_2 surface can harness effective transfer of electrons through the TiO_2–C hetero junction, and promote the photocatalytic performance of TiO_2.

© 2012 Elsevier B.V. All rights reserved.

1. Introduction

Photocatalysis has emerged as an indispensable area of research due to the promise of the utilization of abundant renewable resources for a wide variety of applications ranging from tumor cell therapy [1,2] to environmental remediation [3–6], and clean energy production [7–9]. The generation of hydrogen from water in the presence of a photocatalyst is a sustainable approach, which provides an avenue through which energy costs and environmental pollution can be minimized by harnessing of solar energy. Although ideal for energy security, the harvesting of sunlight for the hydrogen generation is still a challenging venture necessitating extensive research and development of advanced technologies. This process requires a chemically stable, non-toxic visible light photocatalyst that can be prepared by simplified scalable methods, and importantly has the ability to separate photogenerated electrons from reactive holes while minimizing energy losses related to charge transfer [10]. Hitherto existing light absorbing materials such as TiO_2 have limitations in the combination of these synergetic properties. Although the wide band gap limits the application of TiO_2 to the UV region, extensive research has demonstrated the ability of this semiconductor to absorb photons of light and generate excitons that migrate to the surface of the photocatalyst, and take part in oxidation and reduction processes [11]. In light activated water splitting, prolonged life time of the electrons is vital to enable the reduction of hydrogen ions to hydrogen. However, the fast decay of electrons causes recombination of charge carriers, which further diminishes the photocatalytic efficiency of the semiconductor [12]. Several strategies have been investigated for the modification of the semiconductor so as to prolong the life time of the electrons and holes and improve the overall photocatalytic activity such as metal ion and anionic doping. Most recently, the incorporation of carbonaceous materials such as carbon black, carbon nanotubes, graphite, and graphene have demonstrated efficient electron accepting capabilities thereby modifying the electron–hole recombination processes in semiconductors. Among the carbonaceous sources investigated, graphene has demonstrated versatility in the improvement of functionality for various semiconductor nanoparticles due to its exceptional charge carrier mobility, thermal and electrical conductivity, optical transmittance, and mechanical stiffness [13–15]. Photocatalytic hydrogen evolution has been realized using P25-reduced graphene (RGO) [16] and $BiVO_4$–RGO composites [17] composites. It has been suggested that the intimate contact between the semiconductor and RGO facilitates the transfer of photogenerated electrons from the semiconductor to the carbon materials and improves the photocatalytic efficiencies.

A scalable synthesis procedure for defect free sp^2 hybridized graphene is still of a major challenge as the existing processes are tedious, expensive, and are limited to nanoscale applications. These methods are based on the oxidation of graphite to graphitic

* Corresponding author. Tel.: +1 605 677 6189; fax: +1 605 677 6397.
E-mail address: ranjit.koodali@usd.edu (R.T. Koodali).

0920-5861/$ – see front matter © 2012 Elsevier B.V. All rights reserved.
doi:10.1016/j.cattod.2012.02.010

oxide by methods developed and verified by Brodie [18], Staudenmaier [19], and Hummers and Offeman [20]. However these procedures entail the use of a combination of strong, potentially hazardous acids such as H_2SO_4, HNO_3, and $HClO_4$. The vastly employed Hummers method [20] is also vulnerable to production of excess permanganate ions that may require treatment by H_2O_2, washing and thorough dialysis in order to minimize contamination of the resultant composite. An additional step to convert graphitic oxide to graphene is necessary and often requires strong reducing agents, such as hydrazine, a highly toxic reagent that imposes health and environmental risks [21]. In respect to these concerns, an alternative safer approach for producing graphene of minimized defects has been through micromechanical exfoliation using scotch tape, and chemical exfoliation in solvents, however the scalability and reproducibility of these methods is still low [22]. An improvement in graphene yield may be achieved by chemical vapor deposition of hydrocarbons such as CH_4 or C_2H_2 gases on reactive nickel or transition-metal-carbide deposited on SiO_2/Si substrates surfaces to produce thin carbon layers. On the contrary, this approach requires the use of an electron beam evaporator and heating at 1000 °C under argon atmosphere that limits its technological application due to the confined use of gaseous raw materials [23]. Epitaxial growth of graphene on semiconducting surfaces such as SiC wafers by vacuum graphitization has been utilized to produce an ultrathin epitaxial carbon species. Although high quality graphene is achieved, it requires expensive electron-beam patterning and development, and oxygen plasma etching under high vacuum conditions [24,25]. In retrospect, these methods involve several steps that increase the chances of introducing defects into the graphene, and as a result dampening their electronic and mechanical properties. Therefore, there is a need to develop simple chemical methods and thus far, investigators have demonstrated the synthesis of carbon materials from alternative inexpensive carbon sources such as small organic molecules by physicochemical modification through pyrolysis. Mesoporous carbon was prepared using silica template and resorcinol–formaldehyde gel [26] and simple sugars such as glucose [27]. However these multistep methods employ highly corrosive HF, and involve the use of surfactants for stabilizing graphene that have a tendency to occlude the active sites of the semiconductor, and retard the mechanical and electronic properties of the resultant graphitic materials [14]. Yamashita and co-workers have deposited carbon on a periodic mesoporous material, TiO_2/MCM-41 using 2,3-dihydroxynaphthalene (DN) as a precursor and studied the degradation of 2-propanol under UV light irradiation [28]. There are other reports in the literature exemplifying photocatalytic activities of TiO_2–C materials synthesized from small organic molecules but our approach is differentiated in that carbonized aperiodic TiO_2 mesoporous materials are prepared by tuning the composition of DN, and studying the effects on the photocatalytic evolution of hydrogen under solar simulated conditions. The development of defect free carbon structures on metal oxide nanoparticles is not a trivial process and although attempts have been made to synthesize these advanced materials, there is still opportunity to improve the quality and yield, and attain materials exhibiting maximized synergetic effects between the C and the metal oxide semiconductor.

2. Materials and methods

2.1. Materials

Titanium isopropoxide ($Ti(^iOPr)_4$, Acros, 98+%), anhydrous ethanol (Pharmco-AAPER, A.C.S./USP grade), 2,3-dihydroxynaphthalene (Acros 98%), methanol (Fisher, ACS grade), conc. nitric acid (Acros, ACS grade). Deionized water (resistivity >18 MΩ m) and the chemicals mentioned above were used without further purification.

2.2. Catalyst preparation

2.2.1. Synthesis of TiO_2

In a typical synthesis 2.2 mL of $Ti(OCH(CH_3)_2)_4$ was added drop wise into a solution containing 9 mL of C_2H_5OH under vigorous stirring in a Teflon liner. The hydrolysis process was initiated by the introduction of 1 mL of H_2O and catalyzed by the addition of 100 μL of conc. HNO_3. The resulting mixture was stirred for 3 h, a time period sufficient for gelation to be achieved. The resultant gel was subjected to hydrothermal treatment in a Thermolyne autoclave reactor furnace and heated to a temperature of 120 °C for 14 h, filtered, and dried overnight at 75° C. The obtained powder was then ground and a portion was calcined at 800 °C and utilized as the bare TiO_2 material (TiO_2-0). The rest of the catalyst was calcined at 500 °C and used for the synthesis of TiO_2–C hybrid material.

2.2.2. Synthesis of TiO_2–C hybrid materials

The selective C-coating of the hydrothermally synthesized TiO_2 nanoparticle surface was performed using 2,3-dihydroxynaphthalene (DN) as a precursor. In two separate reaction vessels, 120 and 240 mg of DN were dissolved in 150 mL acetone. 90 mg of TiO_2 was added to each and the resultant mixtures were stirred at room temperature for 1 h. The clear solution immediately turned orange in this step due to ligand-to-metal charge transfer (LMCT) complex formation. The mixtures were purified by filtration, washed repeatedly with acetone, and then dried at 75 °C overnight. The resultant composite powders were heated at 800 °C at a rate of 3 °C/min for 4 h under N_2 purging, and then cooled gently. The sample turned grey. It was determined that the control of the reaction temperature and N_2 flow rate were critical parameters for effective carbonization of the composite mixtures. The hybrid materials obtained were denoted as TiO_2–C-120 and TiO_2–C-240.

2.3. Catalyst characterization

The samples were characterized by transmission electron microscopy (TEM), powder X-ray diffractometry (XRD), Raman spectroscopy, UV–Visible diffuse reflectance spectroscopy (DRS), and photoluminescence (PL) spectroscopy. TEM images were recorded on a Tecnai G^2 instrument operating at 120 kV. Samples for TEM analysis were prepared by dispersing each material in ethanol, and the suspensions were sonicated for 1 h. One drop of the suspension of each material was placed on a copper grid coated on a carbon film, and allowed to dry overnight. The XRD measurements were performed at room temperature using a Rigaku Ultima IV X-ray diffractometer with Cu Kα radiation operated at 40 kV and 44 mA. The diffractograms were scanned with a step size of 0.02° and at a scan speed of 1°/min in the range of 2θ = 10–80°. The UV–Visible diffuse reflectance spectra were recorded using a Cary 100 Bio UV–Visible spectrophotometer with a praying mantis diffuse reflection accessory (Harrick Scientific). Raman spectra were measured on a Horiba Jobin Yvon Labram Aramis Raman spectrometer with a He–Ne laser (532 nm) as the light source. The unfiltered beam of scattered laser radiation was focused onto the sample through a microscope objective (50×) for an acquisition time of 10 s and repetition of 10×. The radiation was then dispersed by an 1800 line/mm grating onto a CCD detector. X-ray photoelectron spectroscopy was carried out using a custom-designed Kratos Axis Ultra instrument in a surface analysis chamber with monochromatic radiation at 1486.6 eV from an aluminum Kα source using a 500 mm Rowland circle silicon single crystal monochromator.

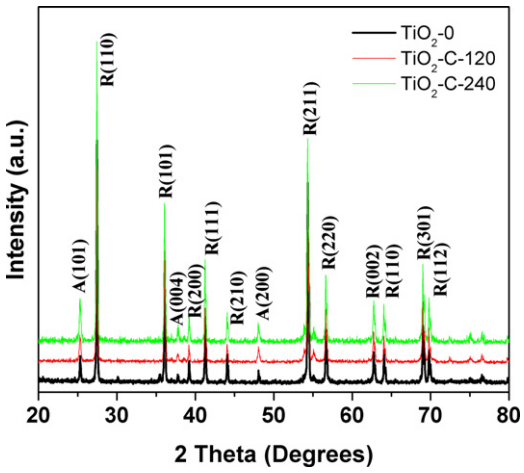

Fig. 1. Powder X-ray diffraction pattern of TiO_2–C hybrid materials obtained from the interaction of TiO_2–DN after pyrolysis. Bare TiO_2-0 is also shown for comparison. A and R refers to anatase and rutile phases of TiO_2, respectively.

The X-ray gun was operating with current at 15 mA and at an accelerating voltage of 15 kV. The textural properties such as surface area and pore size distribution of bare TiO_2 and the C-TiO_2 hybrid materials were measured using N_2 physisorption measurements. After the samples were dried over night at 70 °C and degassed at 100 °C for at least 1 h, N_2 isotherms were obtained at 77 K using a NOVA 2200*e* (Quantachrome Instruments) surface area and pore size analyzer. The surface area was calculated using the Brunauer–Emmett–Teller (BET) equation within a relative pressure range (P/P_0) of 0.05–0.30. The pore volume was determined from the amount of N_2 adsorbed at the highest relative pressure of $P/P_0 \approx 0.99$. The pore diameter and pore size distribution plots were defined by applying the Barrett–Joyner–Halenda (BJH) model to the desorption isotherm. PL measurement was carried out on a Horiba Jobin Yvon-Fluoromax4. The excitation wavelength used was 280 nm, and the emission spectra were monitored in the range of 400–600 nm.

2.4. Photocatalytic water splitting

Photocatalytic hydrogen evolution reactions were carried out in a 5 mL quartz reactor similar to a previous study reported by our group [29]. Typically, 0.002 g of the catalyst was suspended in a solution of 1.6 mL of H_2O and 0.4 mL of methanol. A 300 W xenon lamp equipped with an optical transmission filter >280 nm was used as the AM 1.5 simulated light source. The suspension was sonicated for 1 min and degassed for 30 min with high-purity argon in order to eliminate dissolved oxygen prior to solar simulated light irradiation. The amount of H_2 produced was measured by gas chromatography (SRI 8610C) equipped with a molecular sieve column and a TCD detector, and using a previously prepared calibration graph.

3. Results and discussion

The formation of TiO_2–C was initialized by (LMCT) complex between the two adjacent phenolic OH groups of DN and TiO_2 [30–32]. Fig. 1 shows the XRD pattern of TiO_2–C hybrids exhibiting diffraction peaks due to highly crystalline rutile TiO_2 (>90%) along with a small percentile of the anatase phase TiO_2 (<10%). The peaks are reflective of d_{110}, d_{101}, d_{200}, d_{111}, d_{210}, d_{211}, d_{220}, d_{002}, d_{110}, d_{301}, and d_{112} at two theta values of 27.5°, 36.1°, 39.2°, 41.23°, 44.2°, 54.3°, 56.7°, 62.9°, 64°, 68.9°, and 69.8°, respectively, indicative of the rutile phase. Anatase peaks due to d_{101}, d_{004}, d_{200}, d_{105}, and d_{204} are observed at two theta values of 25.2°, 37.9°, 48.1°, 55.1°, and 62.8°, respectively. However, the characteristic peak of carbon at 26° is not observed from the hybrid materials probably due to the massing of different oriented carbon regions. Small amorphous carbon particulates attached on the highly crystalline rutile TiO_2 may also render the carbon diffraction peak difficult to be observed [33]. Fig. 2 exhibits the N_2 desorption isotherms of TiO_2–C composites, which provide information about the structural properties and pore geometries of the materials prepared at various compositions of DN. The N_2 isotherms of bare TiO_2 (TiO_2-0), and the materials of low carbon content such as TiO_2–C-120, and TiO_2–C-240 displayed type V isotherms of mesoporous materials that initially experience monolayer adsorption at low relative pressure levels. As the relative pressure increases, multilayer adsorption occurs prior to capillary condensation. They maintain convexity, a feature that suggests relatively stronger lateral interactions between adsorbed molecules than the interactions between the adsorbent and the adsorbate molecules. These materials also exhibit isotherms with Type H3 loops that do not level off at relative pressures close to the saturation vapor pressure indicative of the composition of loose aggregates of plate-like particles forming slit-like pores. The loops are somewhat hybrid in nature experiencing hysteresis along the entire relative pressure range as a result of the combination of thermodynamic and network effects arising from non-coincidental capillary evaporation and condensation within interconnecting pores of various sizes. In addition, hysteresis at low pressures is probably due to swelling of the adsorbent during the adsorption process or the concurrence of physical adsorption and chemisorption processes [34]. An increase in the carbon loading from 120 to 240 mg has no effect on the type V isotherm

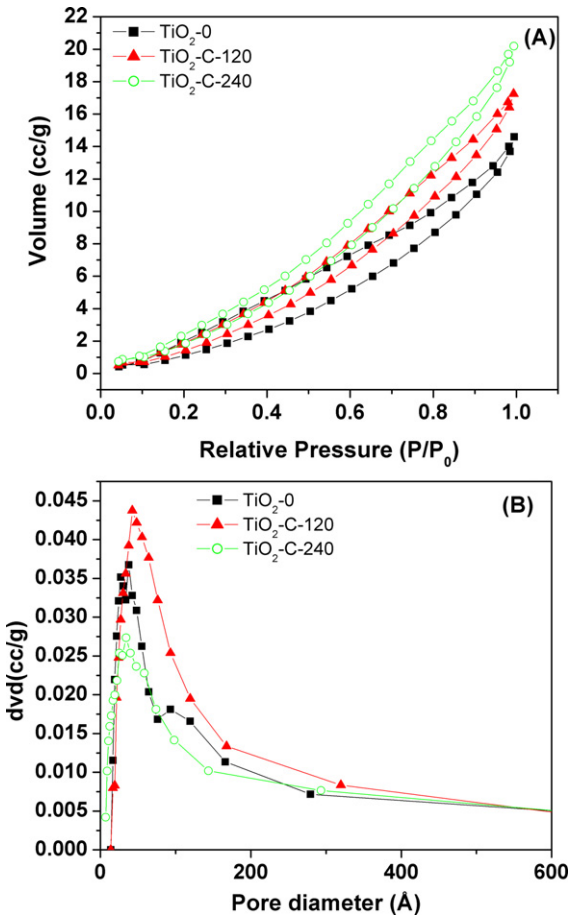

Fig. 2. Nitrogen isotherms (A) and pore size distribution (B) of TiO_2–C hybrid materials.

Table 1
Textural properties of C–TiO_2 hybrid materials obtained from DN.

Materials	S_{BET}[a] ($m^2\ g^{-1}$)	Pore volume ($cm^3\ g^{-1}$)	Ave. pore diameter (Å)	BJH pore diameter[b] (Å)	H_2 evolution ($\mu mol/g_{TiO_2}/h$)
TiO_2-0	6.5	0.02	133	24	~0
TiO_2–GC-120	10.5	0.03	101	27	0.45
TiO_2–GC-240	12.5	0.03	100	38	2.6

[a] Surface area determined by applying Brunauer–Emmett–Teller (BET) equation to a relative pressure (P/P_0) range of 0.05–0.35 of the adsorption isotherm.
[b] Calculated from the Barrett–Joyner–Halenda (BJH) equation using the desorption isotherm.

profile, and mesoporosity is maintained in all the materials prepared. The pore geometries in TiO_2-0 display a bimodal distribution at 27 and 38 Å. The range of pores is narrowed as more carbon is introduced in the TiO_2 matrix with unimodal distributions at 43 Å and 34 Å for TiO_2–C-120 and TiO_2–C-240, respectively. The narrow pore size distribution is reflected in fairly similar surface areas. TiO_2-0 resulted in a material of a low surface area of 6.5 $m^2\ g^{-1}$, which improved slightly after C anchoring to 12.5 $m^2\ g^{-1}$. These changes may be attributed to the anchoring of TiO_2 on the C surface. The textural properties of surface area, pore volume, and average pore diameter obtained from N_2 adsorption–desorption analysis are summarized in Table 1.

Raman spectra were collected in order to provide more information about the structural features of the TiO_2–C composite materials. Fig. 3 shows Raman spectra of TiO_2–C composites derived from DN. The bare TiO_2-0 displays strong bands at 140 cm^{-1} due to anatase and at 235 cm^{-1}, 450 cm^{-1}, and 610 cm^{-1} are ascribed to rutile TiO_2 phases. The incorporation of C features results in the display of two broad bands with intensity maxima close to 1350 cm^{-1} (D band), related to imperfections in the sp^2 carbon structure and associated with A_{1g} symmetry. The band at approximately 1585 cm^{-1} (G band) is associated with the E_{2g} vibrational mode of sp^2 bonded carbon atoms [35]. The position and intensity ratio of these two bands were not influenced by a change in the carbon content. This might be due to the formation of C on the surfaces of TiO_2 nanoparticles via DN–TiO_2 surface complexes. The nature of the interaction between TiO_2 and C was further investigated by XPS. Fig. 4(A) shows the high-resolution XPS spectra of the C 1 s region, taken on the surface of bare TiO_2-0 and a representative TiO_2–C-240. It can be observed that the C 1s spectra span over a broad energy range from 282 to 291 eV. The binding energies at 284.4 eV may be assigned to disordered carbon in the hybrids [36]. The peaks with binding energies at 286.1 and 288.3 eV are attributed to C–O and C=O bonds, respectively, which indicates the formation of carbonated species and a probable substitution of lattice titanium ions to form Ti–O–C bonding [36]. The XPS spectra for the O 1s region of the TiO_2-0 and TiO_2–C-240 materials are illustrated in Fig. 4(B). The binding energies for O–Ti and OH are observed at 529.7 and 531.9 eV, respectively, in the TiO_2-0 material whereas the TiO_2–C-240 material results in corresponding peaks at 529.6 eV and 531.9 eV. It also appears that the content of surface hydroxyl groups is much lower in the TiO_2–C-240 than that

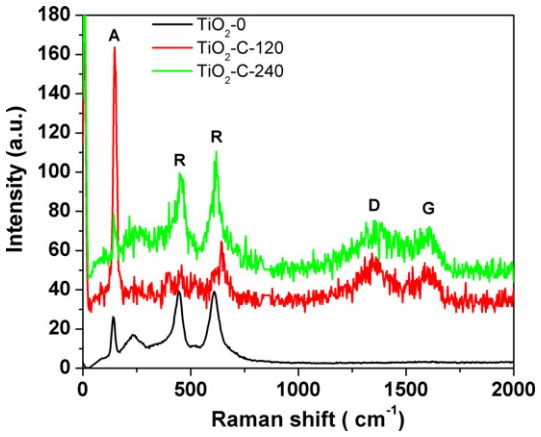

Fig. 3. Raman spectra of TiO_2–C hybrid material. Bare TiO_2 (TiO_2-0) is also shown for comparison. A and R refers to anatase and rutile phase of TiO_2 and D and G refers to the A_{1g} and E_{2g} characteristic of carbon.

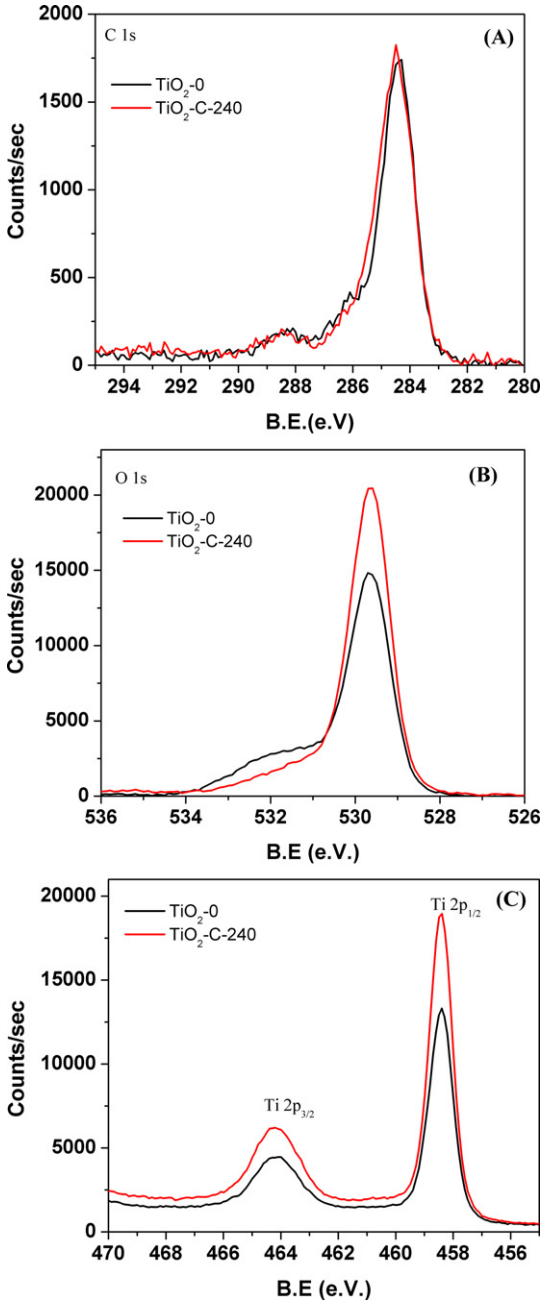

Fig. 4. XPS spectra of bare TiO_2-0 and a representative of the TiO_2–C hybrid material, TiO_2–C-240.

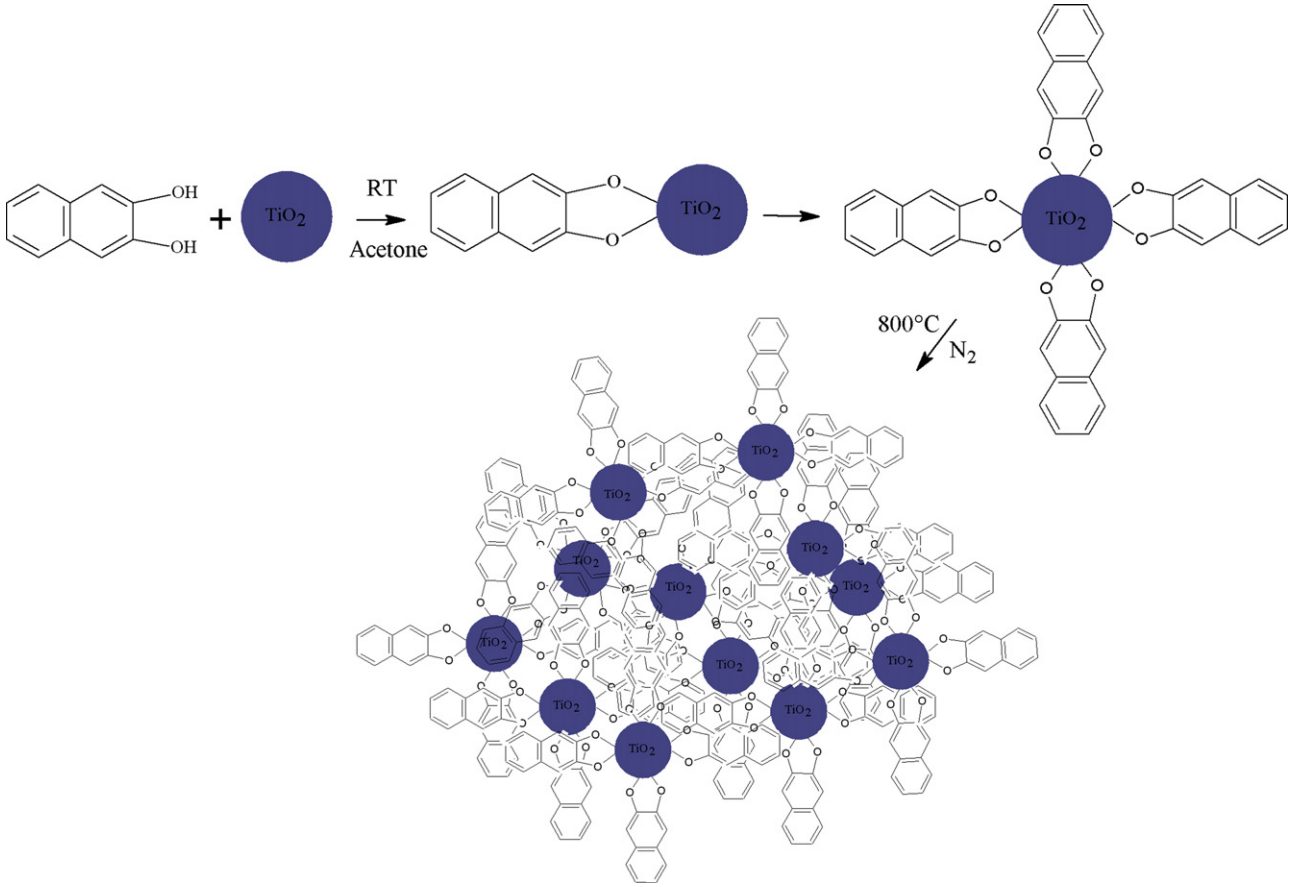

Scheme 1. Proposed mechanism to illustrate the coordination between OH groups of DN with the surface of the TiO_2 nanoparticle during carbonization process.

in the TiO_2-0 attributed to the complex formation of TiO_2 with C. The peaks corresponding to the binding energies at 458.4 eV and 464.1 eV are due to Ti 2p emerging with $2p_{3/2}$ and $2p_{1/2}$ spin orbit pairs. This is indicative of fully oxidized titanium to form TiO_2 [37] in the TiO_2-0 and TiO_2–C-240 materials as shown in Fig. 4(C). An increase in peak intensity for the carbonized material is indicative of the exposure of Ti atoms after the cleavage of surface hydroxyl groups due to the formation of C resulting from pyrolysis. The interaction of C and TiO_2 is further investigated by observing diffuse reflectance spectra of the resultant materials as illustrated in Fig. 5. TiO_2-0 exhibited a large optical absorption band below 380 nm corresponding to the band-gap energy of TiO_2 primarily in the UV region. The effective band gap estimated from the onset of absorption clarifies that the band gap of TiO_2 is maintained at around 2.9 eV even after the incorporation of carbon. The loss of intensity of absorption is also a unique result and could be attributed to the formation of layered carbon structures that impede the penetration of the UV light from sensitizing the embedded semiconductor particles. This observation sparked an investigation into the coordination of the material before and after carbonization. When TiO_2 was treated with an acetone solution of DN, the solution turned orange, depicting strong LMCT complexation. The complex formed exhibited absorption in the visible light region around 450–700 nm prior to pyrolysis (spectrum shown in inset of Fig. 5). The formation of DN–TiO_2 surface complexes presumably occurred through the reaction of Ti–OH with the hydroxyl groups on DN. The electronegativity for TiO2 is 1.54 and for carbon (graphitic) Diebold and co-workers studied the binding configuration of catechol OH groups on the TiO_2 surface [38]. They determined the likelihood that both OH groups dissociate and the O binds to a surface Ti atom in a bidentate configuration through proton exchange with the surface. Eder and Windle utilized benzyl alcohol (BA) as a surfactant in the preparation of carbon-nanotube/TiO_2 and they inferred the coordination of BA hydroxyl groups with titanium to form Ti–O–Ti network [39]. Shkrob used IR spectroscopy and XANES to probe the complexation between chemical OH groups of polyols and uncoordinated titanium sites, which results in the formation of Ti^{IV}–O–R groups [40]. We believe that the OH groups on DN coordinate with the surface of the TiO_2 nanoparticle in a similar fashion during carbonization as illustrated in Scheme 1. TEM images were collected

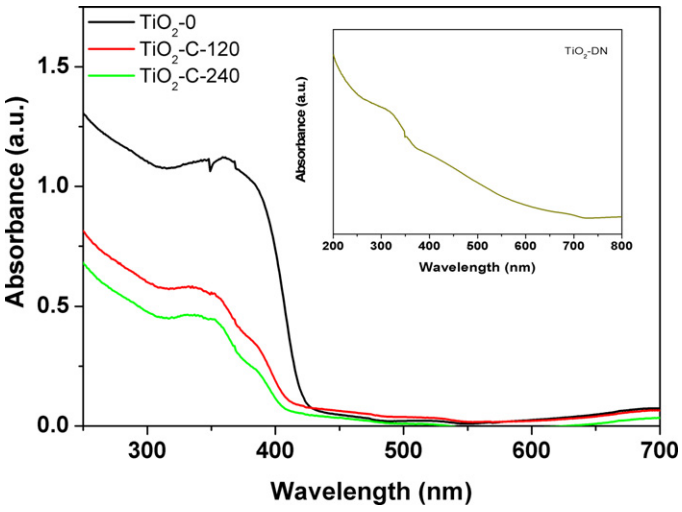

Fig. 5. Diffuse reflectance spectra of bare TiO_2-0 and TiO_2–C hybrid materials. TiO_2–DN LMCT complex formed prior to pyrolysis is also shown in the inset.

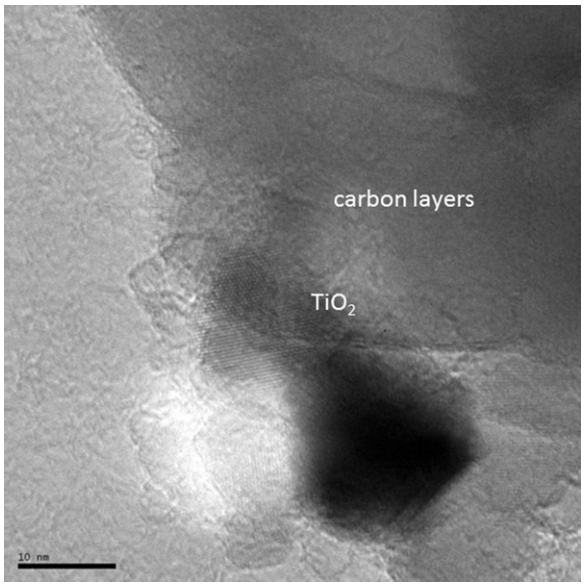

Fig. 6. TEM image of a representative of the TiO_2–C composites, TiO_2–C-120. TiO_2 nanoparticles are observed as lattice fringes.

for a representative material, TiO_2–C-120, in order to probe the morphology of the carbon materials prepared in this study and are shown in Fig. 6. It appears that TiO_2 nanoparticles were present on the carbon layers in a disordered manner probably due to the high temperature transformation of anatase to rutile. The average diameter of the TiO_2 particle was determined to lie between 15 and 20 nm within the carbon that are stacked together and exist as several micrometers in size.

The photocatalytic H_2 evolution results for TiO_2-0 and the hybrid materials (TiO_2–C-120, TiO_2–C-240) each in an aqueous suspension with methanol as sacrificial agent (electron donor) are shown in Fig. 7. The experiment was conducted under solar simulated irradiation (AM 1.5). The bare TiO_2-0 did not generate any H_2 from 0.002 g of photocatalyst even after 10 h of irradiation. However, the incorporation of carbon features resulted in an enhancement of photocatalytic activity for TiO_2–C-120 generating 4.5 $\mu mol/g_{TiO_2}$ of H_2. Doubling the C content led to a marked increase in the production of H_2 to 25.7 $\mu mol/g_{TiO_2}$ highlighting the role of the carbon as an electron acceptor. The generated electrons are transported through the C layers that minimize electron–hole recombination that results in the availability of more electrons to participate in the reduction of H^+ to H_2 [41]. As the carbon content increases, electron propagation through the carbon is promoted and consequently H_2 evolution is enhanced. This was investigated further using photoluminescence spectroscopy. Emission spectra were collected and plotted in Fig. 8 for the materials excited at 280 nm and monitored in the range of 400–600 nm. They exhibited an emission band at 467 nm, attributed to the charge-transfer transition from Ti^{3+} to oxygen anion in a TiO_6^{8-} complex associated with oxygen vacancies at the surface [42,43]. After the formation of TiO_2–C, the fluorescence of TiO_2 was quenched drastically. The PL quenching may have originated from contributions of higher rutile content or the presence of C as an electron acceptor. Recently Baiju et al. [44] reported that PL intensity of TiO_2 decreases with an increasing amount of the rutile. When anatase-TiO_2 is in contact with rutile-TiO_2, photo-induced holes in anatase-TiO_2 accumulate in rutile-TiO_2 while the photo-induced electrons remain in anatase-TiO_2 due to band bending at the interface. This results in an effective charge-separation and increased photo induced e^-–h^+ (excitons) life-time depicted by a reduction in the PL intensity for materials of higher rutile content. Alternatively, charge transfer of photoexcited electrons from the conduction band of TiO_2 to the empty electronic states of C at the TiO_2–C heterojunction may have resulted in non-radiative decay of the TiO_2 excited state [45,46]. The addition of more C to TiO_2 led to further quenching of the this luminescence band probably due to increased electron shuttling from the TiO_2 to the C, thus confirming electron transfer from the semiconductor to the carbon network through the Ti–O–C complexation [47]. It is imperative to acknowledge the contribution of C to charge separation as it possesses efficient electron acceptor properties due to its conjugation structure and its presence has demonstrated higher hydrogen evolution efficiencies in this study.

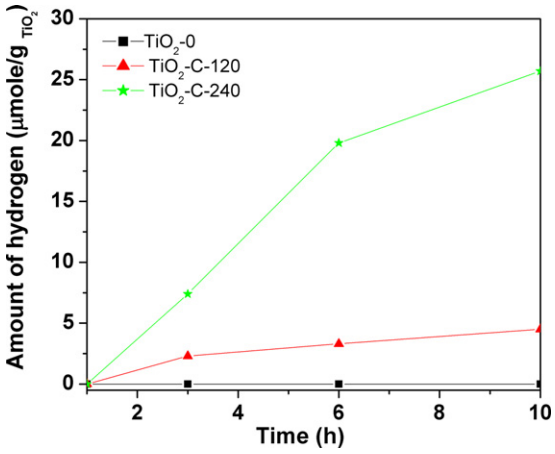

Fig. 7. Photocatalytic hydrogen evolution from TiO_2–C composite materials.

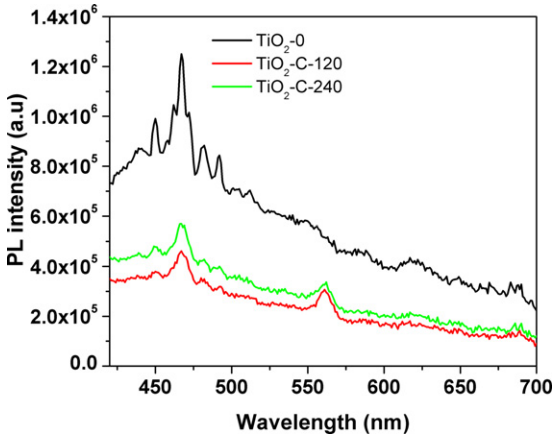

Fig. 8. PL spectra of bare TiO_2-0 and TiO_2–C hybrid materials. Excitation wavelength used was 280 nm.

4. Conclusions

We have prepared highly active carbonized TiO_2 composite materials from a small organic molecule carbon precursor 2,3-dihydroxynaphthalene. The obtained materials exhibited high photocatalytic activity for evolution of hydrogen under simulated solar irradiation. H_2 production was achieved from the carbonized TiO_2 material evolving at rates as high as 2.6 $\mu mol/g_{TiO_2}/h$ from 0.002 g of TiO_2–C-240 after 10 h of irradiation. These results indicate that the presence of C allows faster electron propagation and facilitates electron shuttling through C thus minimizing electron–hole recombination and enhancing hydrogen evolution. This work creates opportunities for the preparation of novel catalytic materials from C using simple methods, and the application

of such photocatalysts for the development of clean energy technology.

Acknowledgments

This work was supported by DE-EE 0000270, NSF-CHE 0840507, NSF-CHE 0722632, and State of SD. We are thankful to Dr. C.Y. Jiang for help with Raman spectrometry analysis, Dr. Jonas Baltrusaitis and Prof. V.H. Grassian for XPS analysis, and Dr. C. Lin for TEM analysis.

References

[1] R. Cai, Y. Kubota, T. Shuin, H. Sakai, K. Hashimoto, A. Fujishima, Induction of cytotoxicity by photoexcited TiO_2 particles, Cancer Research 52 (1992) 2346–2348.
[2] J.W. Rasmussen, E. Martinez, P. Louka, D.G. Wingett, Zinc oxide nanoparticles for selective destruction of tumor cells and potential for drug delivery applications, Expert Opinion on Drug Delivery 7 (2010) 1063–1077.
[3] W. Choi, Pure and modified TiO_2 photocatalysts and their environmental applications, Catalysis Surveys from Asia 10 (2006) 16–28.
[4] M.R. Hoffmann, S.T. Martin, W. Choi, D.W. Bahnemann, Environmental applications of semiconductor photocatalysis, Chemical Reviews 95 (1995) 69–96.
[5] H.S. Kibombo, D. Zhao, A. Gonshorowski, S. Budhi, M.D. Koppang, R.T. Koodali, Cosolvent-induced gelation and the hydrothermal enhancement of the crystallinity of titania–silica mixed oxides for the photocatalytic remediation of organic pollutants, Journal of Physical Chemistry C 115 (2011) 6126–6135.
[6] H. Tahiri, N. Serpone, R. Le van Mao, Application of concept of relative photonic efficiencies and surface characterization of a new titania photocatalyst designed for environmental remediation, Journal of Photochemistry and Photobiology A: Chemistry 93 (1996) 199–203.
[7] A. Fujishima, K. Honda, Electrochemical photolysis of water at a semiconductor electrode, Nature 238 (1972) 37–38.
[8] S. von Kraemer, K. Wikander, G. Lindbergh, A. Lundblad, A.E.C. Palmqvist, Evaluation of TiO_2 as catalyst support in Pt–TiO_2/C composite cathodes for the proton exchange membrane fuel cell, Journal of Power Sources 180 (2008) 185–190.
[9] W. Zhengbang, H. Tang, P. Mu, Self-assembly of durable Nafion/TiO_2 nanowire electrolyte membranes for elevated-temperature PEM fuel cells, Journal of Membrane Science 369 (2011) 250–257.
[10] R.M. Navarro Yerga, M.C. Álvarez Galván, F. del Valle, J.A. Villoria de la Mano, J.L.G. Fierro, Water splitting on semiconductor catalysts under visible-light irradiation, ChemSusChem 2 (2009) 471–485.
[11] A. Jaroenworaluck, W. Sunsaneeyametha, N. Kosachan, R. Stevens, Characteristics of silica-coated TiO_2 and its UV absorption for sunscreen cosmetic applications, Surface and Interface Analysis 38 (2006) 473–477.
[12] J.Z. Zhang, R.H. O'Neil, T.W. Roberti, Femtosecond studies of photoinduced electron dynamics at the liquid–solid interface of aqueous CdS colloids, Journal of Physical Chemistry 98 (1994) 3859–3864.
[13] A.H. Castro Neto, F. Guinea, N.M.R. Peres, K.S. Novoselov, A.K. Geim, The electronic properties of graphene, Reviews of Modern Physics 81 (2009) 109–162.
[14] O.C. Compton, S.T. Nguyen, Graphene oxide, highly reduced graphene oxide, and graphene: versatile building blocks for carbon-based materials, Small 6 (2010) 711–723.
[15] D. Wang, D. Choi, J. Li, Z. Yang, Z. Nie, R. Kou, D. Hu, C. Wang, L.V. Saraf, J. Zhang, I.A. Aksay, J. Liu, Self-assembled TiO_2–graphene hybrid nanostructures for enhanced Li-ion insertion, ACS Nano 3 (2009) 907–914.
[16] W. Fan, Q. Lai, Q. Zhang, Y. Wang, Nanocomposites of TiO_2 and reduced graphene oxide as efficient photocatalysts for hydrogen evolution, Journal of Physical Chemistry C 115 (2011) 10694–10701.
[17] Y.H. Ng, A. Iwase, A. Kudo, R. Amal, Reducing graphene oxide on a visible-light $BiVO_4$ photocatalyst for an enhanced photoelectrochemical water splitting, Journal of Physical Chemistry Letters 1 (2010) 2607–2612.
[18] B.C. Brodie, On the atomic weight of graphite, Philosophical Transactions of the Royal Society of London 149 (1859) 249–259.
[19] L. Staudenmaier, Verfahren zur Darstellung der Graphitsäure, Berichte der Deutschen Chemischen Gesellschaft 31 (1898) 1481–1487.
[20] W.S. Hummers, R.E. Offeman, Preparation of graphitic oxide, Journal of the American Chemical Society 80 (1958) 1339-1339.
[21] E. Ruiz-Hitzky, M. Darder, F.M. Fernandes, E. Zatile, F.J. Palomares, P. Aranda, Supported graphene from natural resources: easy preparation and applications, Advanced Materials 23 (2011) 5250–5255.
[22] H. Kim, A.A. Abdala, C.W. Macosko, Graphene/polymer nanocomposites, Macromolecules 43 (2010) 6515–6530.
[23] K.S. Kim, Y. Zhao, H. Jang, S.Y. Lee, J.M. Kim, K.S. Kim, J.-H. Ahn, P. Kim, J.-Y. Choi, B.H. Hong, Large-scale pattern growth of graphene films for stretchable transparent electrodes, Nature 457 (2009) 706–710.
[24] C. Berger, Z. Song, X. Li, X. Wu, N. Brown, C. Naud, D. Mayou, T. Li, J. Hass, A.N. Marchenkov, E.H. Conrad, P.N. First, W.A. de Heer, Electronic confinement and coherence in patterned epitaxial graphene, Science 312 (2006) 1191–1196.
[25] K.S. Novoselov, A.K. Geim, S.V. Morozov, D. Jiang, Y. Zhang, S.V. Dubonos, I.V. Grigorieva, A.A. Firsov, Electric field effect in atomically thin carbon films, Science 306 (2004) 666–669.
[26] S. Han, T. Hyeon, Simple silica-particle template synthesis of mesoporous carbons, Chemical Communications (1999) 1955–1956.
[27] J.-S. Yu, S.B. Yoon, G.S. Chai, Ordered uniform porous carbon by carbonization of sugars, Carbon 39 (2001) 1442–1446.
[28] T. Kamegawa, D. Yamahana, H. Yamashita, Graphene coating of TiO_2 nanoparticles loaded on mesoporous silica for enhancement of photocatalytic activity, Journal of Physical Chemistry C 114 (2010) 15049–15053.
[29] D. Zhao, S. Budhi, A. Rodriguez, R.T. Koodali, Rapid and facile synthesis of Ti-MCM-48 mesoporous material and the photocatalytic performance for hydrogen evolution, International Journal of Hydrogen Energy 35 (2010) 5276–5283.
[30] N.M. Dimitrijevic, T. Rajh, Z.V. Saponjic, L. de la Garza, D.M. Tiede, Light-induced charge separation and redox chemistry at the surface of TiO_2/host–guest hybrid nanoparticles, Journal of Physical Chemistry B 108 (2004) 9105–9110.
[31] N.M. Dimitrijevic, Z.V. Saponjic, D.M. Bartels, M.C. Thurnauer, D.M. Tiede, T. Rajh, Revealing the nature of trapping sites in nanocrystalline titanium dioxide by selective surface modification, Journal of Physical Chemistry B 107 (2003) 7368–7375.
[32] T. Rajh, L.X. Chen, K. Lukas, T. Liu, M.C. Thurnauer, D.M. Tiede, Surface restructuring of nanoparticles: an efficient route for ligand-metal oxide crosstalk, Journal of Physical Chemistry B 106 (2002) 10543–10552.
[33] Z. Lei, Y. Xiao, L. Dang, W. You, G. Hu, J. Zhang, Nickel-catalyzed fabrication of SiO_2, TiO_2/graphitized carbon, and the resultant graphitized carbon with periodically macroporous structure, Chemistry of Materials 19 (2006) 477–484.
[34] M. Kruk, M. Jaroniec, Gas adsorption characterization of ordered organic–inorganic nanocomposite materials, Chemistry of Materials 13 (2001) 3169–3183.
[35] A. Sadezky, H. Muckenhuber, H. Grothe, R. Niessner, U. Pöschl, Raman microspectroscopy of soot and related carbonaceous materials: spectral analysis and structural information, Carbon 43 (2005) 1731–1742.
[36] W. Zhongbiao, D. Fan, Z. Weirong, W. Haiqiang, L. Yue, G. Baohong, The fabrication and characterization of novel carbon doped TiO_2 nanotubes, nanowires and nanorods with high visible light photocatalytic activity, Nanotechnology 20 (2009) 235701.
[37] S. Chakraborty, M.K. Bera, P.K. Bose, C.K. Maiti, Analysis of interface states of Al/TiO_2/$Si_{0.3}Ge_{0.7}$ MIS structures using the conductance technique, Semiconductor Science and Technology 21 (2006) 335–340.
[38] S.-C. Li, J.-G. Wang, P. Jacobson, X.Q. Gong, A. Selloni, U. Diebold, Correlation between bonding geometry and band gap states at organic–inorganic interfaces: catechol on rutile TiO_2(1 1 0), Journal of the American Chemical Society 131 (2009) 980–984.
[39] D. Eder, A.H. Windle, Carbon–inorganic hybrid materials: the carbon-nanotube/TiO_2 interface, Advanced Materials 20 (2008) 1787–1793.
[40] I.A. Shkrob, M.C. Sauer, D. Gosztola, Efficient, rapid photooxidation of chemisorbed polyhydroxyl alcohols and carbohydrates by TiO_2 nanoparticles in an aqueous solution, Journal of Physical Chemistry B 108 (2004) 12512–12517.
[41] H. Zhang, X. Lv, Y. Li, Y. Wang, J. Li, P25-graphene composite as a high performance photocatalyst, ACS Nano 4 (2009) 380–386.
[42] F.B. Li, X.Z. Li, The enhancement of photodegradation efficiency using Pt–TiO_2 catalyst, Chemosphere 48 (2002) 1103–1111.
[43] J.C. Yu, J. Yu, W. Ho, Z. Jiang, L. Zhang, Effects of F-doping on the photocatalytic activity and microstructures of nanocrystalline TiO_2 powders, Chemistry of Materials 14 (2002) 3808–3816.
[44] K. Baiju, A. Zachariah, S. Shukla, S. Biju, M. Reddy, K. Warrier, Correlating photoluminescence and photocatalytic activity of mixed-phase nanocrystalline titania, Catalysis Letters 130 (2009) 130–136.
[45] J. Liu, J. Li, A. Sedhain, J. Lin, H. Jiang, Structure and photoluminescence study of TiO_2 nanoneedle texture along vertically aligned carbon nanofiber arrays, Journal of Physical Chemistry C 112 (2008) 17127–17132.
[46] M. Olek, T. Büsgen, M. Hilgendorff, M. Giersig, Quantum dot modified multiwall carbon nanotubes, Journal of Physical Chemistry B 110 (2006) 12901–12904.
[47] T. Banerjee, S. Rawalekar, A. Das, H.N. Ghosh, Interfacial electron transfer dynamics of two newly synthesized catecholate bound Ru^{II} polypyridyl-based sensitizers on TiO_2 nanoparticle surface – a femtosecond pump probe spectroscopic study, European Journal of Inorganic Chemistry 2011 (2011) 4187–4197.